Original Paper

Landslides
DOI 10.1007/s10346-024-02374-x
Received: 13 February 2024
Accepted: 12 September 2024

Marin K. Clark · Dimitrios Zekkos · John Manousakis

Enabling 3D landslide event statistics using satellite and UAV-enabled topographic differencing

Abstract Knowledge of landslide volumes is needed to connect landslide trigger, geometry, and mechanism with the mechanical characteristics of the displaced soil and rock masses. While landslide volume inventories of widespread events are scarce, increasing availability of high-resolution imagery time-series presents new opportunities for developing volume inventories in terms of scale and resolution. Here we present a novel 3D landslide volume dataset using topographic differencing methods to evaluate the potential for such studies in future hazard and geomorphic research. Remotely sensed stereo optical imagery collected shortly after the 2015 Lefkada M_w6.5 earthquake event in western Greece was used to create two post-event DSM surfaces using Worldview-3 satellite images with the SETSM algorithm and UAV-based optical imagery using Structure from Motion (SfM). We demonstrate good agreement between methods for mapping of ~ 700 landslides. Elevation change more accurately identifies source areas on steep slopes compared to imagery alone, distinguishes deeper landsliding from shallow ravel, and reveals complex patterns that are not well approximated by simple landslide slip surface geometries. Statistical relationships are sensitive to aspects of the methodology, namely topographic resolution, accurate image registration, and estimation of 2D (plane) area versus 3D surface area. These analyses also raise the question of what constitutes a single landslide mass in these events and thus the utility of landslide frequency as a statistical measure. As we achieve resolution that surpasses ground-based field studies and removes the selection bias of focusing only on select well-defined, deep landslides, new patterns of ground failure emerge to which mapping and statistical data interpretations will need to adapt.

Keywords Landslide inventory · Co-seismic landslides · DEM differencing · Photogrammetry

Introduction

Landslides are complex geologic phenomena that displace rock and/or soil downslope causing significant hazard in many environments across the world. Widespread landslide events are commonly triggered by large earthquakes or intense storms, which cause hundreds to tens of thousands of landslides (Malamud et al. 2004) of varied failure mechanisms (Varnes 1978; Hungr et al. 2014). Under these conditions, slope failure is induced by horizontal seismic accelerations or changes to the hydrodynamic regime of the near surface respectively resulting in a range of landslide sizes that span many orders of magnitude. Generally speaking, the volume of an individual landslide will dictate how far the slide mass travels, how it interacts with other hillslope materials, and how it contributes to sediment loading in nearby colluvial and fluvial channels. As such, measuring and predicting the size and location of landslide triggering provides insight to material properties and landslide mechanics where knowledge of the forcing event can be estimated. Importantly, these data can be used to classify landslide type and mechanism (Alberti et al. 2022), to assess material properties of the shallow subsurface or conditions (e.g., water pressures, external loads) at failure through back-analysis (Kallimogiannis et al. 2019, Bunn et al. 2020, Gong et al. 2021, Alberti et al. 2022), as well as to assess runout potential and downslope effects (Costa and Schuster 1988; Crosta et al. 2003; McDougall 2017; Fan et al. 2020). Increased focus on the landslide-sediment cascade has highlighted the importance of landslide connectivity to river systems, particularly in understanding how the volume and grain size of landslide debris affect channel morphology and conveyance capacity, which can in turn lead to increased flooding hazards.

While such assessment of landslides on an individual basis is often used in engineering, the forefront of study for landslide mechanics involves analysis of large landslide populations of hundreds to thousands of simultaneous landslides over large geographic areas that can result in geospatial estimates of strengths and landslide risk across larger regions. These events present new opportunities, albeit with some challenges. For example, estimates of landslide volume form the basis of slope stability back analysis, as well as their mobility, both of which are critical considerations when assessing infrastructure resiliency (Postance et al. 2017, Miele et al. 2021). Back-analysis of landslides can be used to derive material parameters and the conditions (e.g., water pressures, external loads) under which the landslide occurred (Alberti et al. 2022). These events provide the opportunity to make these calculations under similar conditions, across regional gradients in surface properties and can provide necessary input to estimation of future slope hazards (Jones et al. 2023).

However, measurement of the size of the displaced slide mass, failure plane, and material properties are notoriously time-consuming and therefore expensive. Current practice uses a small number of landslides investigated by field studies at best because depth measurements are time-consuming and therefore by necessity sample only a relatively small fraction of the total landslide population. Typically, this subset of measurements is used to develop a volume-area relationship that is then extrapolated to a complete inventory of 2D (plan view) mapped areas from imagery (e.g., (Larsen et al. 2010). However, this approach can have a selection bias toward larger, deeper landslides. For example, investigations conducted through the early 2000s generally relied on relatively basic surveying equipment such as measuring tape and a levelling

rod (e.g., Wieczorek et al. 1985, Barnard et al. 2001, Gabet and Dunne 2002). Most studies that detail their field techniques simplify landslide geometry to an ellipse, measuring the major and minor axes to estimate scar area, and multiplying by an average depth to derive volume. It has been noted that this simplification is somewhat subjective and crude for landslides with rough or complex source regions, leading a minority of studies to instead measure longitudinal segments within the source area (May 2002; Imaizumi and Sidle 2007).

Considering the possibly thousands of individual landslides, measurements of landslide geometry present a technological challenge because such studies require high-resolution detail of the land surface before and after the event, and detailed measurement of subsurface properties, typically from invasive exploration (e.g., boreholes) or geophysics, both of which are rarely available. Benchmark datasets that include accurate volume estimates from large landslide events following earthquakes and storms are only recently emerging as high-resolution repeat topography imaging becomes more commonplace (Massey et al. 2020a, b). As imagery datasets have become more commonly available for mapping landslide inventories, visual, and automated methods have been developed that compare before and after optical or radar imagery from landslide-triggering events (Hölbling et al. 2017; Alvioli et al. 2018; Roback et al. 2018; Amatya et al. 2019, 2021; Burrows et al. 2019; Massey et al. 2020a, b; Catani 2021). As such, much knowledge has been gained about the geospatial characteristics of landslide populations. Comparison between digital elevation models (direct differencing of DEMs) that were created before and after a landslide event, is an advancement to field-based measurements of landslide volumes (Kerle 2002; Tsutsui et al. 2007; Lacroix 2016; Massey et al. 2020a, b). DEM differencing, or subtraction of pre- and post-landslide DEMs, allows one to calculate volumes for any arbitrary landslide geometry, and over a larger, more representative area than field expeditions could ever reasonably cover. Such differencing of topography allows for estimation of volume for landslides that have mostly or completely evacuated material from their source plane. However, errors associated with poor geo-referencing and/or thick vegetation coverage in addition to the resolution of pre-event DEM are significant challenges (Kerle 2002; Tsutsui et al. 2007; Martha et al. 2010; Lacroix 2016). While increasing availability of stereo-satellite imagery and UAV imagery for the generation of post-event topography from photogrammetry methods has fueled many new datasets, further analysis is needed to better explore the influence of data type and quality, as well as assessment of differencing calculations.

The availability of high-resolution pre- and post-event topography for a moderate earthquake event in the island of Lefkada in western Greece offered the opportunity to advance topography differencing methods and landslide mapping for 3D landslide geometries using emergent methods for rapidly acquiring cheap DEM difference models (Zekkos and Clark 2019). While these models lack the precision of LiDAR, the ability to rapidly deploy such techniques after a disaster and the substantially lower cost make these methods promising applications in hazard research (Zekkos et al. 2018b) and would greatly expand datasets for geomorphic study. In this paper, we develop two post-event topographic datasets available for this event and explore a range of differencing algorithms to detect surface change and calculate landslide volume. A landslide inventory was developed using before and after satellite imagery with field verification and is used as a part of this study. Products of the topographic differencing were then investigated for inventory area and volume statistics and geospatial relationships, with particular attention to criteria that can be used to identify individual landslides and the resulting metrics commonly used to describe large landslide event inventories.

The 2015 M_w6.4 Lefkada earthquake event

In recent decades, two strong earthquakes in 2003 and 2015 associated with the Kefalonia-Lefkada Transform Fault in western Greece, produced damage in this area with associated large landslide events and liquefaction in the port of Lefkada. Slip along a sub-vertical dextral fault was manifested in the 2015 earthquake, which occurred on November 17, 2015, 07:10 GMT (09:10 local time) and is estimated to be M_L 6.0/M_w 6.5 at a depth of 11 km (Ganas et al. 2015, 2016). The epicenter of the earthquake is located onshore of the island, to the north of the port village of Vasiliki (Fig. 1). The focal mechanism suggested motion on a fault plane oriented parallel with the western coast of the island. The recorded PGA at the town of Vasiliki was 0.37 g in the North–South direction, whereas in the town of Lefkada it was 0.10 g in the North–South direction and lower in the East–West direction. The US Shakemap (vers 2) is a relatively well-constrained model using station data in the vicinity of the landslides that provide an improved estimate of ground motions. Developed by USGS, this version incorporates strong motions recorded in three stations provided by the Institute of Engineering Seismology and Earthquake Engineering (locally known in Greece as ITSAK) in Greece including Chortata, Aghios Nikitas, Lefkada town, and Vasiliki town stations (Fig. 1, Supplementary Information). Peak ground accelerations in the area affected by the landslides (along the coastline), varied from 0.25 to 0.35 g and peak ground velocities varied from 27 to 45 cm/s. These ground motions were concentrated over the steep western coastline of the island and generated ~ 700 landslides during the timespan of the earthquake.

Methods and datasets

A 2.5D DEM was used in the analyses to make pre-/post-earthquake surface comparisons by topographic differencing. The pre-earthquake DEM was generated in 2015 for the Hellenic Cadastre as a photogrammetric sub-product of orthophoto creation from aerial photo strips for the whole region of Greece with a ground sampling distance of 2-m pixel size. The geometric accuracy of the product is RMSEz ≤ 2.00 m and absolute accuracy ≤ 3.92 m for a confidence level of 95%. The raster DEM was converted to a 3D point cloud LAS format to be compatible with 3D spatial products extracted from UAV surveys for 3D terrain analysis (for point cloud density see Supplementary Information Table S2). Two post-earthquake DSM datasets were generated using (1) Unmanned Aerial Vehicles (UAVs) equipped with optical cameras and Structure from Motion (SfM) algorithms, deployed shortly after the earthquake along the majority of the western coastline (November 2015 and April 2016), and (2) satellite stereo imagery and an open-source code (SETSM) which was developed to extract DSMs from paired orthoimages collected a month after the earthquake along the entire coastline (December 2015) (Fig. 1).

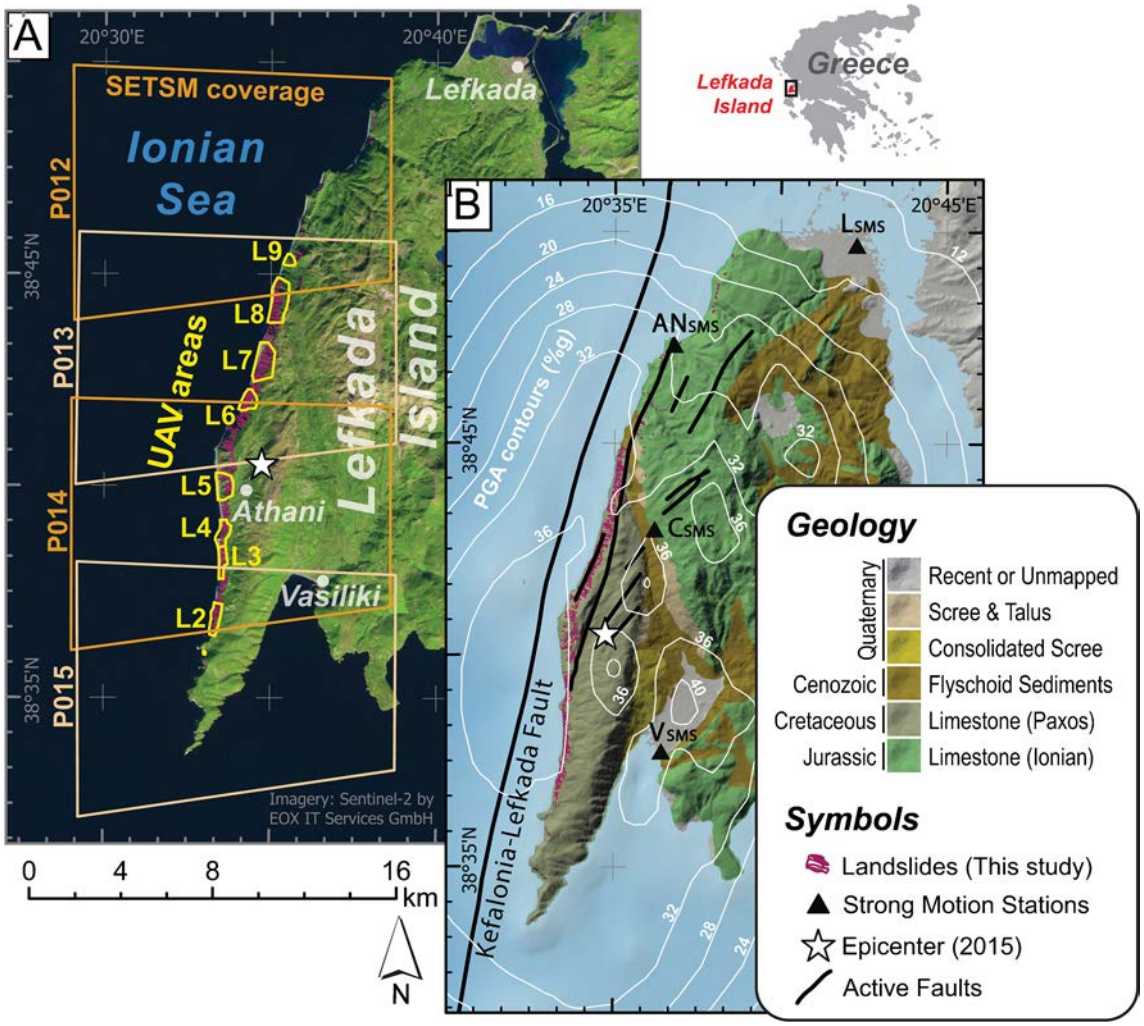

Fig. 1 (**A**) Satellite and UAV DSM coverage. (**B**) Geologic setting of the 2015 M_w6.5 Lefkada earthquake

Post-event topography: generation of UAV datasets

We leveraged field data generated from deployments using quadrotor Unmanned Aerial Vehicles (UAVs) equipped with optical cameras over nine areas of interest along the western coastline (Fig. 1). The imagery was collected using manual controlled gridded flight paths and was stitched together to create 3D models. For the first deployment date on November 19, 2015, only one disaster-affected area (Egremni beach L3/4) was mapped by capturing video using DJI's Phantom 2 Vision + quadrotor equipped with a 14 MP 1/2.3″ image sensor camera. For the rest of the deployment dates, nine areas were mapped along the western coast of Lefkada using DJI's Phantom 3 Pro, featuring a 12.4 MP 1/2.3″ image sensor camera, (April 13, 2016) (Zekkos et al. 2017), capturing 4 K videos along manually controlled gridded flight paths. Extracted frames from video clips for the SfM reconstruction stage maintain 70% side and 80% front overlap. Video capturing was the selected acquisition method due to drone limitations in battery capacity and transmission range. This method allowed for covering larger areas in less time during each flight. Subsequent deployments that were not part of the focus of this paper, were conducted fully autonomously using photo imagery collected on a gridded pattern and had comparable results. The location of the UAV study areas is shown in Fig. 1. Fast-static GPS measurements of ground control points with an absolute coordinate accuracy of 1–2 cm were conducted for some of the surveyed areas, mostly along the top of the landslide areas where access was possible. No GCPs could be measured near the bottom, along the coastline, due to accessibility issues. For fast-static measurements, the Trimble 5800 L1/L2 GNSS receiver was used. Greek Grid coordinate system was implemented for all measurements and converted to WGS84 UTM 34N projection for compatibility with satellite imagery.

Terrain analysis conducted for each site comprises of the extraction of 3D Point Clouds and orthophotos and DSMs using the Structure-from-Motion (SfM) photogrammetric and computer vision methodology with overlapping optical imagery (still photos or video frames) collected using the UAVs as input (Fig. 2). The SfM methodology is a well-established technique (Ullman 1979; Snavely et al. 2008; Westoby et al. 2012), with applications to topographic differencing to infer geomorphic

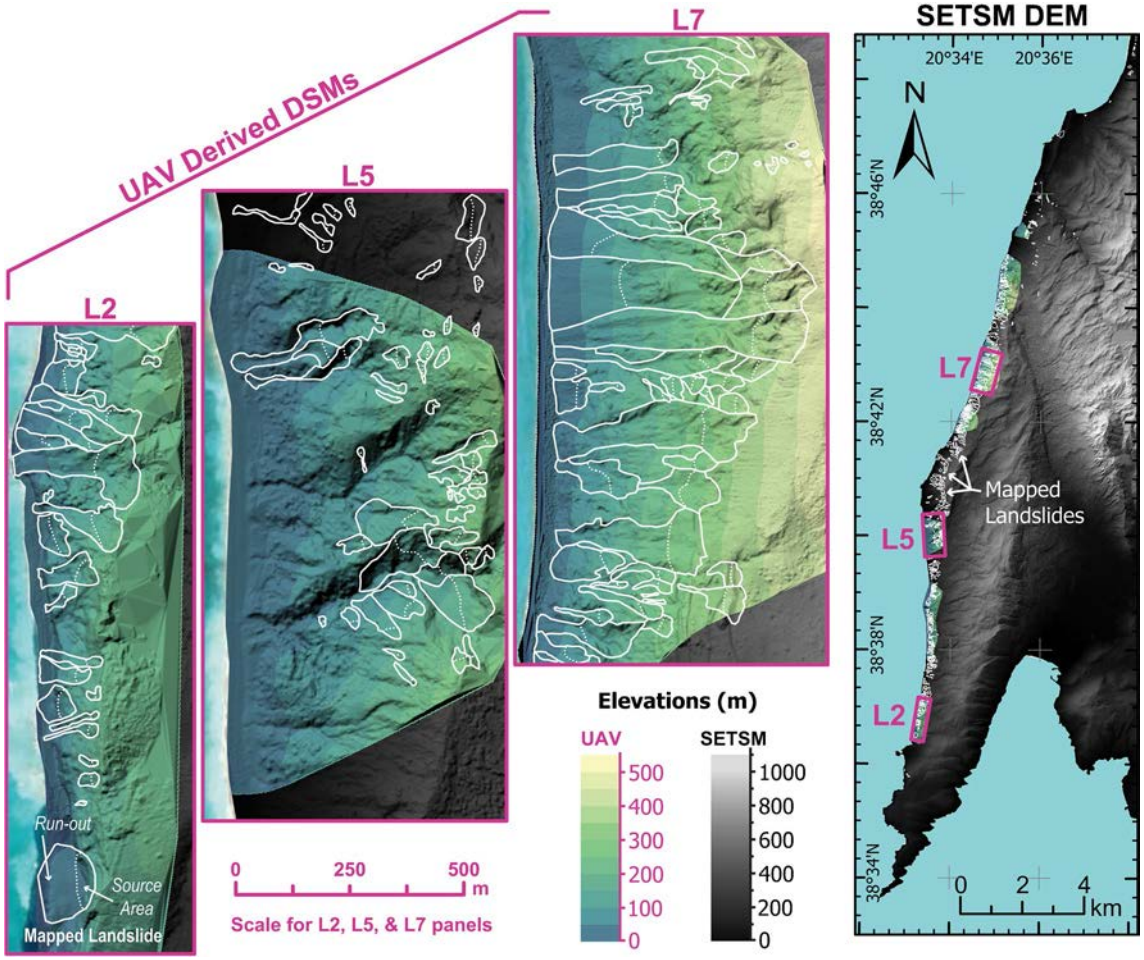

Fig. 2 DSM models derived from UAV and satellite imagery data. Examples of 2.5D DSMs from three of the eight mapped UAV areas. Extraction of 3D Point Clouds, orthophotos, and DSMs used Structure-from-Motion (SfM) methodology with overlapping optical imagery collected using the UAVs as input. Satellite imagery collected by the Worldview-3 satellites by Digital Globe Inc. after the earthquake, on December 28, 2015, was also used for the creation of post-earthquake DSMs with a Ground Sampling Distance (GSD) of 10–30 cm. Four stereo-pairs covering the west coast of Lefkada were used in this study (as shown in Fig. 1). The resolution of the imagery was 30–50 cm allowing for identification of landslide features that are at least 10 m^2 in average dimension

processes (Fonstad et al. 2013; Mancini et al. 2013) and to track displacement of single large landslide complexes (Niethammer et al. 2012, Lucieer et al. 2014). Its specific implementation in this study site has been described in detail in (Zekkos 2018b). The process involves detecting and matching common features as keypoints across multiple overlapping images, estimating the relative positions and orientations of the cameras, and using triangulation to reconstruct the location of 3D points. This process involves intersecting the lines of sight (rays) from the camera centers through the keypoints in the images. Bundle adjustment optimizes the 3D reconstruction and camera parameters to minimize re-projection errors, which refer to the difference between the observed and predicted image positions of the 3D points. For improved accuracy and geo-location, ground control points (GCPs) can be used. These points are established in the field and identified throughout the photoset. The final step uses stereo-matching techniques to generate a dense point cloud or mesh from the sparse set of reconstructed points, where texture mapping can be optionally applied for detailed and realistic 3D models. Ground sampling distance for the spatial products generated ranges from less than 10 cm near the top of the slope to ~ 30 cm due to the significant terrain elevation changes (of about 200 m on average).

Post-event topography: generation of satellite-based DSM (SETSM)

Satellite imagery collected by the Worldview-3 satellites by Digital Globe Inc. (now Maxar) about one month after the earthquake, on December 28, 2015, was used for the creation of post-earthquake DSMs and for interpreting and identifying co-seismic landslide polygons. Four stereo-pairs covering the west coast of Lefkada were used in this study (as shown in Fig. 1). The resolution of the imagery

was 30–50 cm allowing for identification of landslide features that are at least 10 m² in average dimension.

For DSM extraction, the open-source Surface Extraction with TIN-based Search-space Minimization (SETSM) methodology (vers. 3.2.7) developed by (Noh and Howat 2015, 2017) was implemented, which is based on a combination of the vertical line locus method (Schenk 1999) and an adjustment of the rational polynomial coefficients that describe the satellite orbit to produce surface models. The SETSM algorithm has been applied previously for development of the ArcticDEM, enabling glacier change detection studies from topographic change models (Abdullah et al. 2015; Dai et al. 2018). Recent applications of the SETSM algorithm in geoscience include geomorphology (Atwood and West 2022, Corsa et al. 2022), volcanology (Dai et al. 2022), and glaciology (King et al. 2020, Melling et al. 2024). The SETSM methodology has been implemented and described previously by the authors for surface fault and landslide displacements in the Kaikoura 2016 earthquake in New Zealand (Zekkos et al. 2018a). Four 0.5-m raster resolution DSMs were created and cropped inside the area of interest, as shown in Fig. 1A.

A major issue when performing analyses using 3D models generated with SfM and SETSM is that the model includes all visible features, including vegetation and structures, and these features may obscure the bare earth ground. In this study, vegetation within the landslide areas and along the steep coastline was sparse. Still, two different vegetation removal algorithms were tested to create bare earth models (DTMs) for all UAV- and SETSM-mapped areas. To assess how accurately the various algorithms remove vegetation, a sample area within the UAV 3D point cloud was selected and vegetation points were manually classified carefully to compare the results to the vegetation removal algorithms. The sample 3D Point Cloud was derived with 2 classes, vegetation and bare earth ground (Fig. 3).

The first algorithm that was tested is fully automatic and relies on Agisoft Metashape SfM's software machine learning techniques to automatically classify points in various classes (high vegetation, low vegetation, buildings, ground, roads, etc.). No training of the algorithm was required and the classification results can only be altered manually. By running the classification tool for the sample area, only top parts of large trees were classified as vegetation, leading to poor classification results for ground and vegetation points, as shown in Fig. 3. The second algorithm that was tested is Cloudcompare's CANUPO classifier. CloudCompare is a 3D point cloud open-source processing software and the CANUPO classifier plugin serves as a method to classifying a point cloud. The CANUPO classification algorithm relies on geometric characteristics of features and not RGB attributes of the points. The user manually creates unique classifiers (by training them on small samples) and/or applies one classifier at a time on the point cloud to separate it into two subsets. To train the classifier, polygons from vegetated areas and clear terrain were selected with an effort to select representative polygons of the real asset class (small and large elements, different species, different ground cover, etc.). The classifier is then executed with previous training sets generating for each point in the cloud, two scalar fields: one for the class and an additional with the classification "confidence" value for each point so that the user can quickly identify problematic cases. The CANUPO classification method was also implemented for the SETSM dataset within the

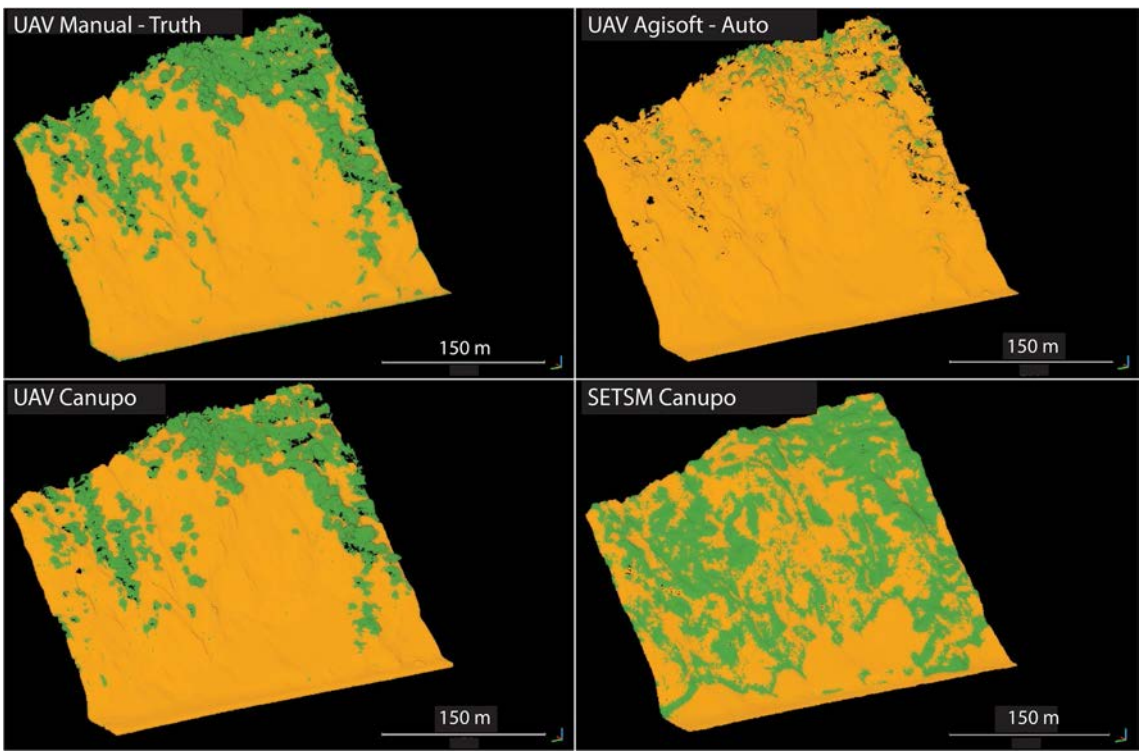

Fig. 3 Classification comparison between Agisoft UAV, CANUPO UAV, and CANUPO SETSM

same sample area. The lower dataset resolution (50 cm) compared to the UAV point cloud (~ 10 cm) and noisy SETSM output made it more challenging to geometrically classify ground and vegetated areas. For the UAV point cloud, CANUPO performed relatively well, though some sparse noise points remain inside the vegetation class that required cleaning to create the Digital Terrain Model. CANUPO generally outperformed classification based on RGB and HSV color filters, which left outlier and generally noisy results.

Further optimization is possible by improving training sets, identifying more classes and better-selecting object scale samples. The Agisoft Metashape automatic classification algorithm on the UAV data did not perform well with problems probably associated with resolution of model and the steepness of the terrain. When applied to the SETSM point cloud, CANUPO classification did a poor job identifying vegetation points, mostly due to lower resolution dataset and due to the challenges in selecting characteristic sample polygons for terrain and vegetation. Removing vegetation from this dataset results in a point cloud with large holes, leading to significant coarsening of the resulting Digital Terrain Model. A detailed qualitative and quantitative evaluation of the different classification techniques was made using confusion matrices and various metrics of success such as accuracy, positive predictive value, negative predictive value, recall r, specificity, and F1 score, and this work is described by Zekkos and Clark (2019). On the basis of the results, the CANUPO classifier was implemented to remove vegetation from all UAV 3D point clouds. Data gaps left by vegetation removal were filled by triangulation during the 3D TIN creation in ArcMap. For the SETSM datasets, it was decided not to remove vegetation, because of (a) the poorer CANUPO classifier results that would cause large gaps in the digital elevation model; and (b) the errors associated with vegetation were not considered critical for volume calculation of landslides because steep slopes have sparse to no vegetation based on imagery and field inspection.

2015 landslide event inventory development

Before/after event date imagery from WorldView 3 (Digital Globe, Inc) satellites was the main basis for identifying landslides related to the 2015 earthquake event (Fig. 4) since they covered the entire study area. This imagery provided up to 0.3 m resolution from which changes to surface vegetation, albedo, and roughness were used to identify landslides triggered by the earthquake. Landslide morphology, which included head scarps, slump blocks, debris scour, and debris deposition, were also recognized and used to guide landslide mapping. Detailed perimeter boundaries were manually mapped onto orthorectified, pan-sharpened imagery using GIS software. Over 700 landslides were identified, from which

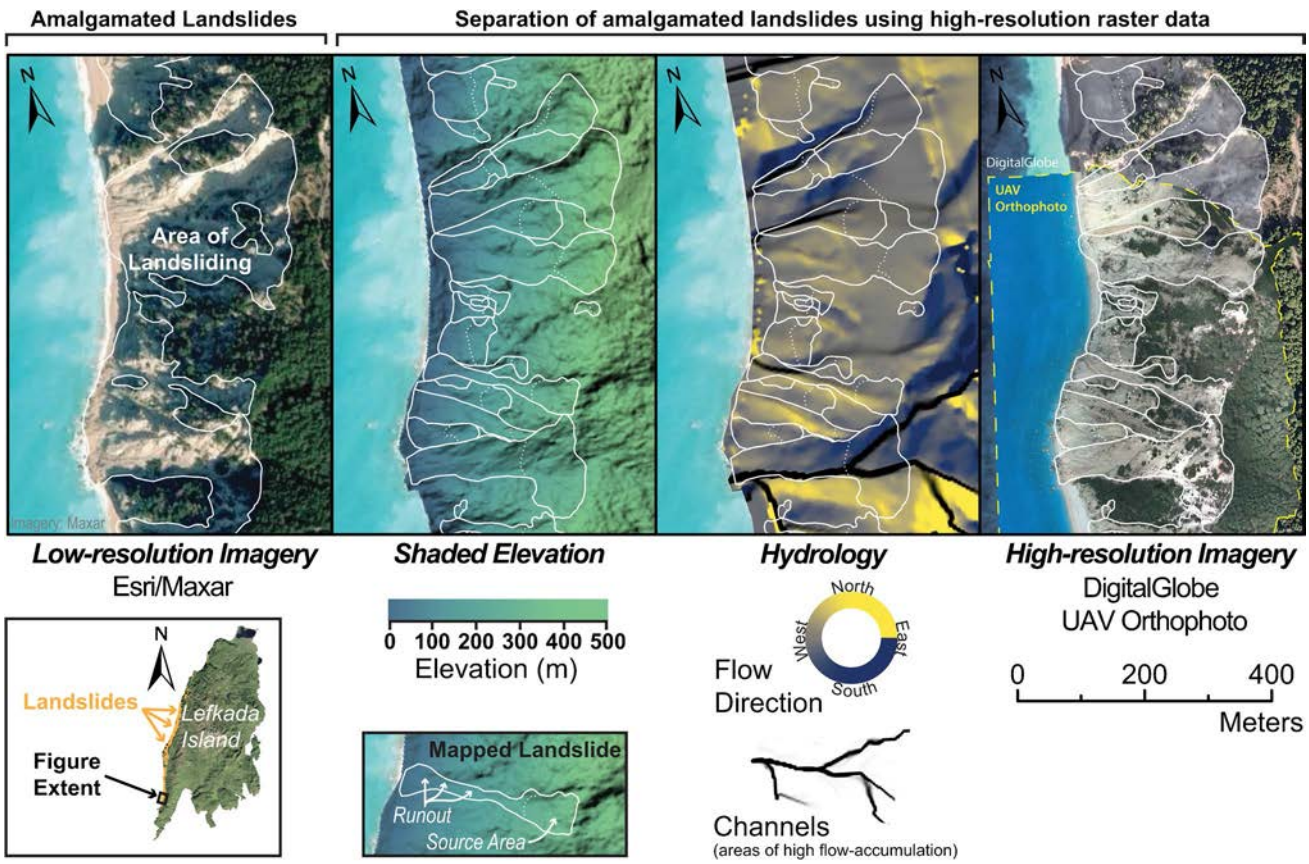

Fig. 4 Landslide inventory development. (left) Low-res satellite imagery depicting contiguous areas of landsliding with amalgamation and no separation between source and runout. (center and right) Raster data derived from the topography model used in combination with hydrologic flow paths, flow direction, and optical imagery to differentiate amalgamated landslides and to define source regions (dashed lines)

both their polygon perimeter (full areas) and source areas were individually mapped.

In areas of dense landsliding, particular attention was paid to the effect of amalgamation (Marc et al. 2015) (Fig. 4). While optical characteristics were the primary criteria used to identify landslides, additional characteristics of the topography (determined from slope, aspect, and flow accumulation rasters) were also used to separate individual landslides by recognizing minor ridge segments in the topography and the orientation of debris scour/deposition (Fig. 4). In addition, cm-scale imagery/ topography from eight areas of UAV survey along the coast, supplemented mapping efforts (Fig. 4). 3D perspectives using a 5-m DEM and UAV-generated topography were also used to identify boundaries between adjacent areas of landsliding. Typically, distinct debris cones could be recognized from which the uphill contributing landslide areas were distinct (Fig. 5). The results from the DEM differencing were also considered in refining landslide boundaries, especially in areas where vegetation was sparse or reactivation of previous landsliding was unclear from imagery alone.

DEM differencing models and landslide volume estimation

Landslide volume estimates were determined from differencing of pre- and post-earthquake surface models and interpreting vertical surface elevation change over the mapped areas of landsliding. Two post-event models (comparison surfaces: UAV and SETSM) were used to develop (1) difference surface models and (2) landslide volume inventories relative to the pre-earthquake Hellenic Cadastre 2 m DEM (2015) as a reference surface. The resulting difference raster represents vertical surface change between the

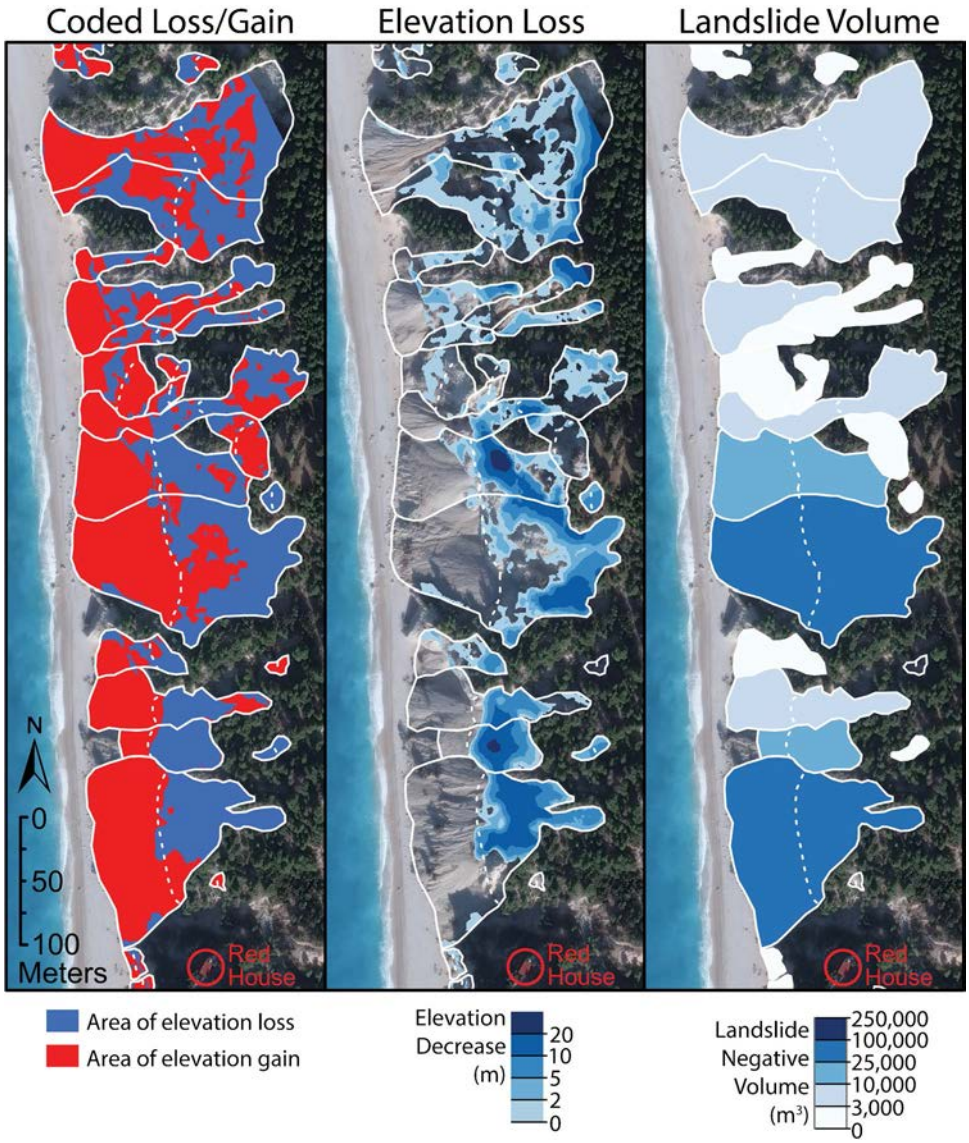

Fig. 5 Example surface difference maps from UAV areas. (left) Coded areas refer to either surface elevation gain loss (blue) or gain (red) in the surface difference map. (center) Elevation loss in landslide source region. (right) Landslide volume summed over total landslide area

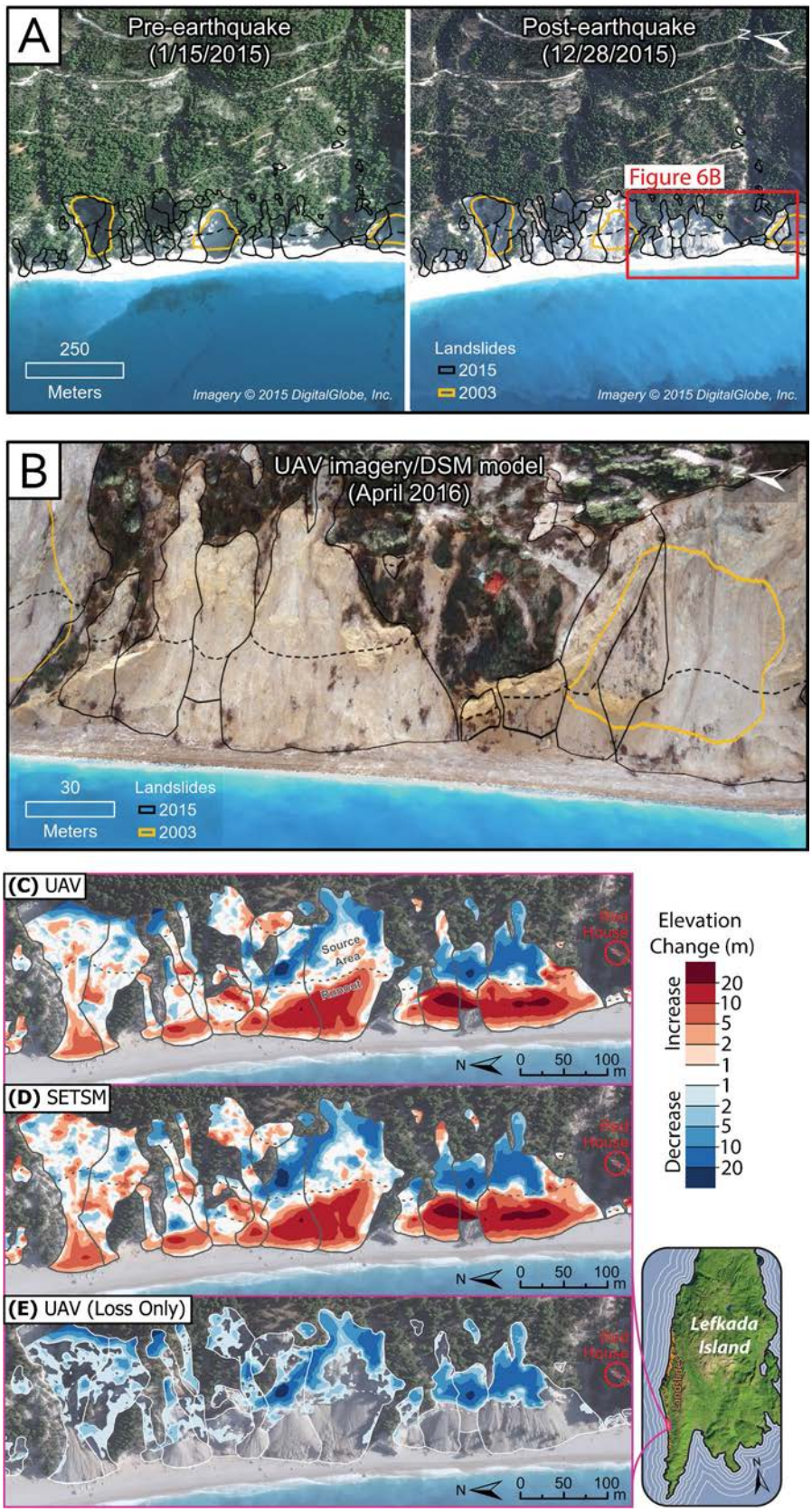
A
Pre-earthquake
(1/15/2015)
Post-earthquake
(12/28/2015)
Figure 6B
250
Meters
Landslides
2015
2003
Imagery © 2015 DigitalGlobe, Inc.
Imagery © 2015 DigitalGlobe, Inc.
B
UAV imagery/DSM model
(April 2016)
30
Meters
Landslides
2015
2003
(C) UAV
Source Area
Runout
Red House
N
0 50 100 m
(D) SETSM
(E) UAV (Loss Only)
Elevation Change (m)
Increase
20
10
5
2
1
Decrease
1
2
5
10
20
Lefkada Island
Landslides

◂**Fig. 6** Before/after imagery and surface difference maps. A Before/after event satellite imagery. B Oblique view of UAV DSM with orthophoto. C, D UAV and SETSM difference maps with mapped landslides. The northern area of the selected area highlights areas of patchy, shallow surface change associated with ravel and shallow rock slides while the southern area is an example of well-defined continuous areas of surface loss/gain associated with deeper rock slides. E UAV—areas of volume loss only within the mapped source areas

two-time instants, which we sum as volume loss due to landsliding (surface lowering) and volume gain due to debris deposition (surface rise) over the areas of mapped landslides from the imagery analysis (Fig. 5). All raster grid models (pre-quake DEM and post-quake SETSM DSM) were converted to 3D point clouds in Cloud Compare, preserving grid resolution, and the pre-quake DEM was also converted to a TIN surface model in Cloud Compare. Both the SETSM and UAV point clouds were registered to the pre-quake TIN in Cloud Compare by first clipping to the approximate area of the reference surface, and then using an Iterative Closet Point (ICP) algorithm—a rigid body transformation that is comprised of a translation and a rotation that minimizes the mean square error between a series of selected pair points. Each UAV area and SETSM scene was aligned individually, with some variation in the resulting goodness of fit between scenes (Supplementary Information). As described previously, vegetation was removed from UAV 3D point clouds using CANUPO classification, but no such filtering was performed on the SETSM models. This method has been used previously for landslide monitoring and mapping tectonic deformation with LiDAR point clouds (Teza et al. 2007, Nissen et al. 2012), but to our knowledge is the first application of the ICP algorithm to a catastrophic landslide event to determine volumes from hundreds of simultaneously generated landslides that form a regional event.

Raster DSMs were then converted to LAS 3D point clouds for 3D terrain analysis with UAV and pre-quake 3D point clouds. SETSM 3D point cloud registration was performed by applying a transformation based on the Iterative Closest Point (ICP) method in Cloud Compare, using the pre-quake Hellenic Cadastre 3D point cloud as reference surface. This method calculates a rigid body transformation between two terrain models that minimizes the closest point distances between them as defined by a matrix composed of translations (t_x, t_y, and t_z in the x, y, and z directions) and rotations (α, β, and γ about the x, y, and z axes). The transformation matrix is then applied to the target point cloud and the point-wise difference between the reference and the transformed point cloud is calculated.

The accuracy of the difference models was evaluated by calculating the mean and standard deviation of the elevation change (more details are given in the Supplementary Information). We considered slopes between 40 and 50° slope, which are the most frequent slope bin that experienced landsliding in this event. We also note that uncertainty increases with increasing slope as small horizontal offsets are magnified by increasing slope values. Mean difference values for the UAV sites range from -0.08 - 0.95 m and standard deviations of 1.44 - 3.12 m, except for L2 (Supplementary Information). The SETSM scenes had slightly larger positive mean offsets (1.27 - 2.21 m) with standard deviations of 2.92–5.17 m. Most areas are normally distributed with a few areas showing positive skewness. Slight positive offsets are expected since we are differencing DSM models with a DEM. The DSM models likely retain some values that represent vegetation or other positive surface features that are above the true ground surface. We were able to successfully apply vegetation filters to the UAV regions whereas the filtering of the SETSM was not successful; therefore, it may be expected that the SETSM have slightly larger positive offsets (and greater standard deviation values) than the UAV models.

Aligned datasets were differenced using the ESRI ArcMap software 3D surface differencing tool to determine areas of elevation gain/loss. This tool creates 3D TIN surfaces from the point cloud, or raster models, and then calculates vertical differences between the two surfaces. The advantage of this tool is that it easily calculates 3D (slope-oriented) area as well as plan-view 2D area for each landslide polygon, which allowed for assessment of 3D slope-areas in the area-volume ratios. Because the UAV and SETSM models have significantly higher resolution than the pre-quake DEM, we set the resolution of the resulting 3D TIN to the resolution of the pre-quake DEM (2 m), and further note that the resolution of the DEM affects the resulting 3D area where increasing resolution (roughness) results in larger 3D areas. The 3D differencing tool gives quantitatively similar volumes to a direct differencing method, where point clouds are interpolated to raster formats and landslide volumes are computed from the summation of the raster elevation differences calculated over each grid cell within the polygon boundary. The resulting surface difference model is coded as either surface loss or gain and were used to sum areas of landsliding and debris deposition respectively. From the surface difference model, we produced (1) a surface difference raster, (2) a summation of negative volumes for each mapped full landslide polygon, and (3) a summation of negative volumes for each mapped source landslide polygon. Additionally, we also calculated the (4) area of only the negative volume that lies within each mapped landslide polygon. Landslide volume uncertainty was calculated using the uncertainty of the difference model (on a per grid cell basis) assuming that the uncertainty of the elevation values are uncorrelated (Supplementary Information). Based on a Monte Carlo sampling model, we note that the volume uncertainty scales as a function of the square root of landslide area and that low volume to area ratio (i.e., thin landslides with ratios of < 0.4) rather than low area alone correlate with large errors 50–400% and are excluded from further analysis (Supplementary Information).

Results

Surface differencing and landslide volumes

Mapped landslide depth varies considerably from less than 1 m to areas with more than 20 m elevation loss from both UAV and SETSM models, and with a similar range of elevation gain associated with debris deposition (Fig. 6). These elevation changes equate to several orders of magnitude landslide volume from 10 to 10^5 m^3, with a modal volume of 10^3 m^3. Largely, source areas that are identified from imagery match broadly as areas of elevation loss in the difference model, and debris trails map as areas of elevation gain. However, it is worth noting the range of surface changes observed in this event. Some landslides have well-defined areas of continuous surface loss and gain that match the mapped regions (source,

and runout) of individual landslides. Other regions are patchy—meaning that the source region (as defined from optical imagery) is a mixture of smaller regions of elevation loss and elevation gain. These regions tend to have much smaller elevation changes (i.e., less than 5–10 m). We associate these regions of shallow and discontinuous surface change with mostly ravel or collection of spatially complex small rock slides—failure mechanisms that likely differ from the larger more coherent landslides defined by regions of continuous surface elevation loss and gain. These slope failures are eliminated by our subsequent statistical analysis by exclusion of low volume-to-area ratios (< 0.4) (Supplementary Information).

Comparison of post-earthquake DSM results (UAV vs. SETSM models) is consistent but the SETSM data is more noisy (Figs. 6 and 7). Generally, spatial patterns of surface gain/loss are similar between the two models even for detailed patterns of patchy, shallow landsliding (Fig. 6). Mean differences between the two rasters show no systematic shift nor skewness. For example, UAV site L3 has a mean offset of -0.08 m and a std dev of 3.12 m (Fig. 7; Supplementary Information). Typically, differences that are greater than the standard deviation (> 1.2 m) occur in two conspicuous patterns. Positive elevation anomalies (higher in the UAV model compared to the SETSM model) appear as small round patches on hillslopes, which we infer to be related to the difference in vegetation height between the two respective sampling periods (December 2015 vs. April 2016). Negative elevation anomalies occur in the channel (lower in the UAV model compared to the SETSM model), which we interpret as sediment evacuation by fluvial process between the two respective sampling periods (December 2015 for the satellite imagery vs. April 2016 for the UAV imagery). The later interpretation is supported by observations in the successive optical images where the low-order channels were loaded with sediment shortly after the earthquake, many of which can be observed as evacuated in later imagery dates. The comparison of landslide volumes between the two models is also consistent but becomes noisy for small landslide volumes or small areas within larger ones (Fig. 7). For example, across individual landslides, there are identical coherent patterns of surface change as highlighted by a smoothed contour model (Fig. 6). Larger landslides are more consistent between the two models, and difference between the two models increases with decreasing landslide volume with some scatter about a 1:1 line and no systematic bias between the two models (Fig. 7).

Landslide mechanism relative to geology, fault proximity, and ground motions

Failures occurred primarily in the limestone units of the Paxos zone, which dominate the region of landsliding (Fig. 1). Near the northern portion of the study area, limestone units of the Ionian zone limestone also failed. A small portion of the study area covered by Miocene age flysch rocks (sandstones, mudstones, and conglomerates) had few failures, but also notably lower average slopes. Field observations suggest that the rock mass is highly tectonized (intensely fractured) throughout the study area, but not substantially chemically weathered with thin to absent soil cover. Brecciation of the rock mass is especially common where plate boundary fault splays of the Kefalonia-Lefkada transform are exposed along

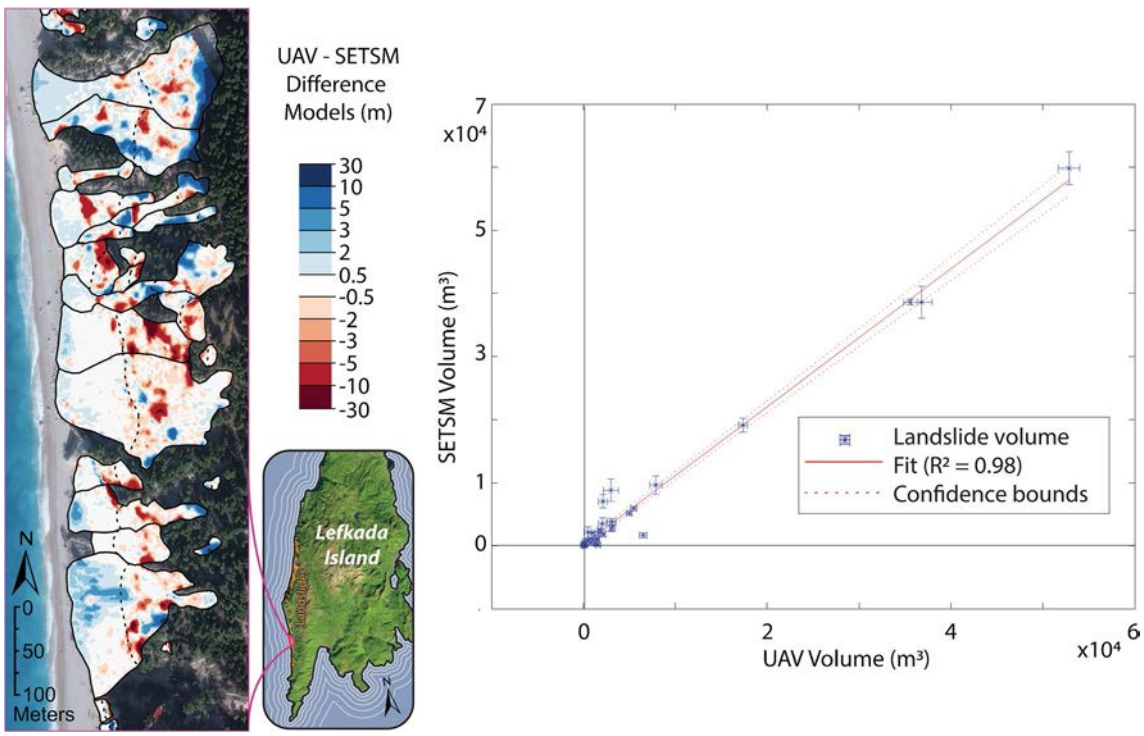

Fig. 7 Comparison of UAV and SETSM models. (left) Orthophotos and DSM difference point cloud for select site L3 ($n = 35$ landslides). Difference values reflect difference between UAV and SETSM post-event topographic models. (right) Landslide volumes from corresponding site

the coast or parallel to the coastline (i.e., near Athani)(Fig. 1). Based on field observations and measured distances to mapped active faults using GIS, fracturing appears to increase with proximity to active structures and likely has a strong influence on the local geotechnical properties of the rock mass (Fig. 8). Such observations are typical of this type of climate-tectonic environment (i.e., relatively dry with seasonal precipitation, highly tectonically active with a high uplift rate and steep coastal retreat rate).

We infer representative landslide mechanisms from landslide geometry and volume, verified by field observation. These include shallow debris and rockslides and occasionally, deep-seated, rotational failures (Fig. 8). Some regions of the coastline had patches of shallow ravel (identified as a change in texture of the ground surface and accumulation of debris in adjacent channel). Some regions of the coast did not fail at all. We identify a sub-set of landslides with well-defined, simple geometries (i.e., a continuous region of surface lowering that is well approximated as an ellipse in the source regions, with corresponding positive regions of debris deposition located downslope) (Medwedeff et al. 2022). These tend to correlate with the deeper landslides, with mean depths of 1 – 10 m. Other landslide regions are typified with a much more complex pattern of surface lowering and irregular landslide area. Notably, many landslides have a complex pattern of volume loss/gain from the difference models as opposed to a simple source/ runout geometry. Such complex geometries typify areas of shallow landsliding (i.e., less than 5 m depth). In some cases, shallow landsliding can be identified in the optical imagery as subtle change in image characteristics in the source region. However, more commonly, shallow landsliding is mainly recognized by new debris deposition observed in nearby stream channels, or debris fans at the base of slopes, because the steep slopes were not vegetated prior to the earthquake and thus visual changes to the source area are difficult to detect. Runout (extent of debris deposition) tends to be constrained by the coastal escarpment, with an unquantified amount of material deposited in the sub-marine environment.

Lithology, strong ground motion, and slope are primary factors that control the frequency and size of co-seismic landslides. Here we consider 2D histogram cross plots of landslide volume compared to peak ground acceleration (PGA), mean and max slope of landslide polygons, and latitude (Fig. 9). Lithology is not considered because nearly all mapped landslides occur in similar composition Mesozoic limestone units (Fig. 1). As with landslide area, volume is lognormally distributed with a characteristic landslide size of about 10^3 m^3, with some skewness toward smaller landslide volumes. When compared to PGA, we discern no pattern with respect to landslide volume but recognize there is narrow range of PGA values over steep topography for this event (0.32 g-0.37 g). Average and maximum slopes within landslide volumes are normally distributed with a slight skewness toward steeper slopes. This produces an overall trend in increasing volume with increasing slope, which is more readily seen in the maximum compared to the mean slope values. Last, we evaluated spatial trends, where latitude is a convenient proxy for distance along the coastal escarpment. Overall, the landslide frequency is highest in the middle of the study area (around 38.70 N) and decreases both to the north and the south. Superimposed on this pattern, there are smaller sub-regions that have correspondingly greater landslide frequency but do not necessarily have greater average landslide volumes.

Landslide inventory statistics

We also consider common statistical measures of the landslide inventory using frequency-area and volume-area relationships.

Fig. 8 Field perspective of volume loss over landslide regions

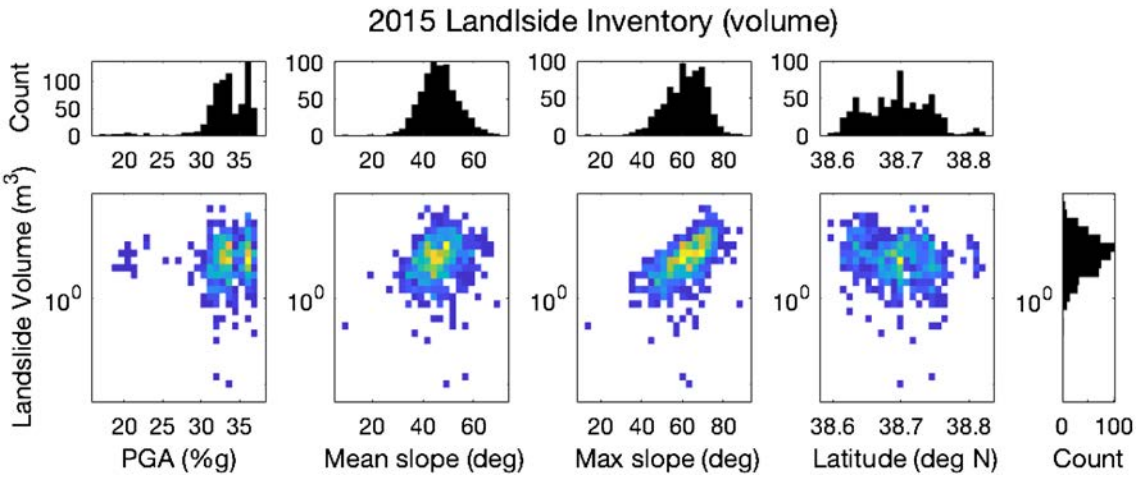

Fig. 9 2D histogram plots of landslide volume vs. PGA, latitude, and max/mean slope for the 2015 event, using the SETSM source volumes. Volume is lognormally distributed with a characteristic landslide size of about 10^3 m^3 (Medwedeff et al. 2020). We also observe no pattern with PGA, albeit that PGA has a narrow range of values for this event. There is no correlation with mean slope, but a positive correlation with maximum slope. There is no discernable pattern between volume and latitude.

Empirical probability density estimates of landslide area distributions for individual event inventories are a typical framework by which we compare different events using a power-law fit to ~ 25% of the largest landslides (e.g., Hovius et al. 1997, Guzzetti et al. 2002, Frattini and Crosta 2013, Tanyas et al. 2017, 2018, Jeandet et al. 2019, Valagussa et al. 2019). However, landslide distributions tend to deviate from power-law behavior at smaller landslide sizes, and empirical probability density bin values are skewed by bin size. Instead, log-normal statistical fits may be more revealing, and thus more apt to investigate details of the decay in landslide frequency at smaller landslide sizes (Medwedeff et al. 2020). A steep decay in landslide frequency at small sizes was thought to be related to image quality in early studies but has more recently continued to be observed for inventories with much higher spatial resolution than the modal landslide size (e.g., Tanyas et al. 2017, 2018), suggesting a physical cause (Medwedeff et al. 2020). Here, the distribution of landslide frequency for the smallest areas is well represented by a log-normal fit (Fig. 10), and we observe a less steep decay in landslide frequency compared to other inventories (Medwedeff et al. 2020) Supplementary Information). We attribute this observation to our high-resolution mapping methods and attention to amalgamation, which may suggest that other inventories still contain some bias at small landslide sizes. Additionally, we observe thin soils and fractured limestone regolith with relatively limited chemical weathering or soil formation. Back-analysis of the landslide inventory using pseudo-3D geometries suggests that the material involved in landsliding has relatively high friction and very low cohesive properties (Gong et al. 2023), which may also contribute to the less steep decay in landslide size frequency for this particular inventory compared to others.

Landslide area-volume relationships for landslides mapped within the areas that have both UAV and SETSM models have statistical properties that are common for mixed soil-rock and rock inventories based on limited number of manually measured landslide volumes (Larsen et al. 2010) (Fig. 11). Typically, inventory data report the plan-view area (2D area) for the entire mapped landslide or less commonly, separately mapped source area (Roback et al. 2018; Massey et al. 2020a, b). Here we additionally consider the 3D area (i.e., sloped area) as well as a summation of area of negative elevation change only within the mapped polygon ("area of negative volume").

We determine a linear relationship between log volume and log area based on different assumptions of area. We exclude very thin landslides (volume/area ratio < 0.4) as these landslides have very high uncertainty and are also likely to have a different mechanism such as raveling or shallow, discontinuous reactivation of previously disturbed material. First, we consider the typical scaling approach of volume versus 2D mapped area of the full landslide using the entire dataset. Unsurprisingly, this yields low exponent values of $\gamma = 1.0$ and intercept values of $\alpha = 0.8$ and 0.9 for the UAV and SETSM models respectively resembling bulk summary statistics from the 2016 M_w7.8 Kaikoura earthquake-triggered landslide inventory (Massey et al. 2020a, b) (Table 1, Fig. 11). Less scatter and steeper relationships are observed when using the 3D source area with exponent values of $\gamma = 1.1$ and intercept values of $\alpha = 0.7$, and even steeper relationships are observed when using the 3D negative source area (γ = 1.2 - 1.6 and α = 0.02 - 0.3) (Table 1; Fig. 11; Fig. 12). Generally there is good agreement between the UAV and SETSM models for most geometries.

The range in log volume-area statistical values demonstrates sensitivity to methodology choices (Table 1). When we consider only the area of negative volume, we produce a steeper and well-defined volume-area relationship by reducing the scatter of low-volume estimates that might be due to debris deposition within the landslide area or complex patterns of amalgamated landsliding in some areas that are not easily separated into independent source regions with corresponding debris trails. The area of negative volume results in smaller areas, because we often observe that volume loss occurs over just a portion of the mapped landslide area. The corresponding results for using the negative area show agreement between the UAV and SETSM models for both sources and full areas. We note in particular, that using only the 3D area of

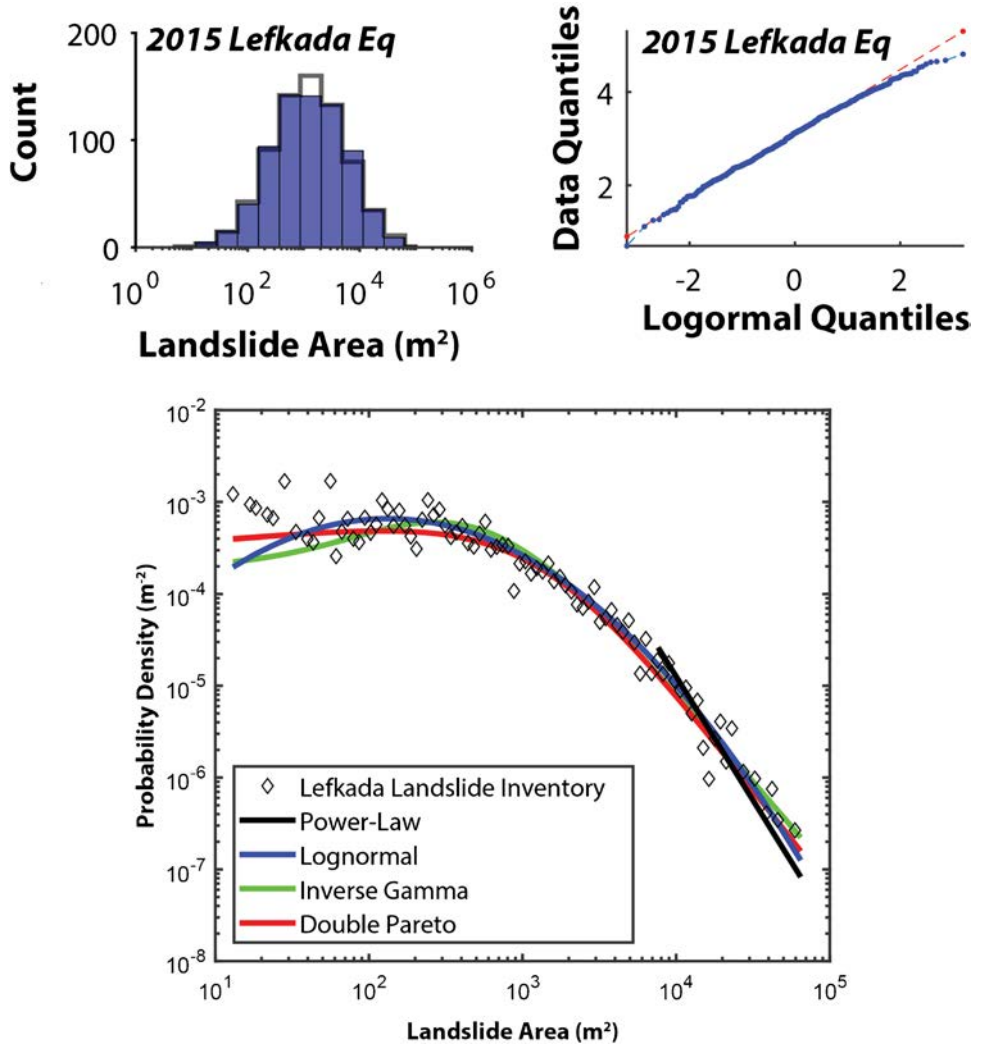

Fig. 10 Landslide frequency-area relationships. Heavy tailed model fits to data from the 2015 landslide inventory (reproduced from Medwedeff et al. 2020)

negative volume produces consistent and steeper values ($\gamma = 1.2$; $\alpha = 0.3$) compared to using the full 3D area ($\gamma = 1.0$-1.1 and $\alpha = 0.7$-0.9) further supporting the observation that areas of patchy, shallow landsliding and ravel introduces complexity to estimating average volume area scaling parameters, even for a single landslide event. This general relationship holds true for source areas and for larger landslides as well.

Discussion

The purpose of this study is to evaluate the use of satellite and optically-derived DSM models for direct measurement of 3D landslide volumes for regionally significant events, which may be more rapidly and cheaply acquired compared to LiDAR and airborne surveys. Comparison of two datasets gives us an idea of the repeatability and reliability of each independent dataset: one from UAV and another from satellites, and each collected on dates a few months apart. The two datasets presented here compare favorably in terms of similarity in spatial patters of elevation loss and gain (Fig. 6) as well as individual landslide volumes (Fig. 7), which suggests that optically derived DSMs are promising for future development of 3D inventory mapping. However, both datasets likely suffer from overestimation of surface change because of vegetation. As expected, we observe a small positive bias in the difference models for both datasets for stable areas (Supplementary Information). We attribute the overall success of the DSM and difference models in Lefkada to the condition of the slopes studied, which are steep and have sparse or no vegetation. While vegetation filtering made some improvement on the UAV models, similar application to SETSM was not successful by the methods presented here. We determine uncertainties on our post-event DSM models to have a mean offset of 0.5 m ($\sigma = 2.1$ m) for the UAV datasets (excluding one region with systematic registration issues) and a mean offset of 1.7 m ($\sigma = 3.5$ m) for the SETSM models. The higher values for SETSM likely reflect in part, vegetation differences compared to the filtered UAV models. Application in more densely vegetated terrain would likely have different results than presented here.

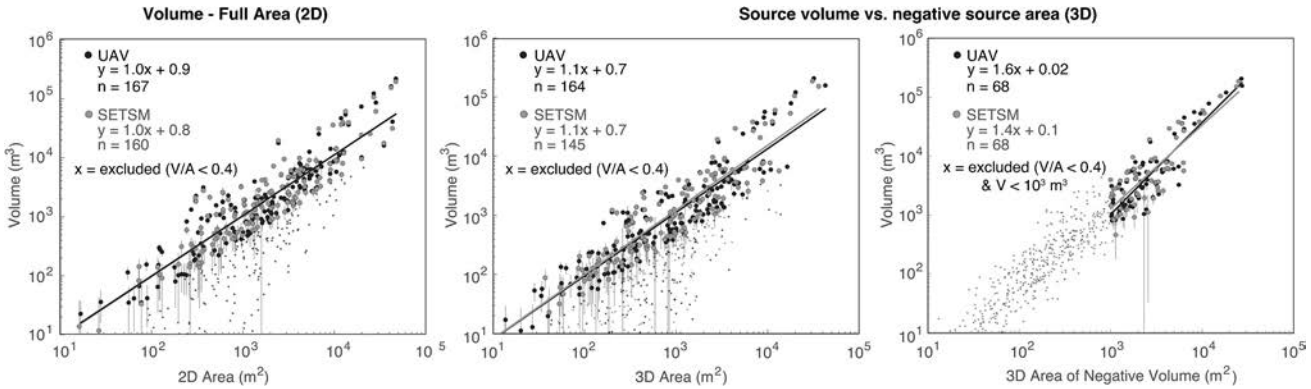

Fig. 11 Volume-area relationships for 2015 coseismic landslides. Volume estimates were based on the integral of surface lowering within each manually mapped full landslide polygon. Landslide area (points) and volume uncertainty (lines) are shown. Transparent values are excluded from regression because of high volume uncertainty (V/A ratio < 0.4). Area-volume scaling relationships take the form of a power law $V = \alpha A^{\gamma}$, where γ is the scaling exponent, and α is the intercept in log space. (left) The area was determined as the 2D or plan view area of the full mapped polygon. (center and right) The area is determined as the summed 3D areas over only regions of elevation loss, i.e., negative areas of the mapped source polygon

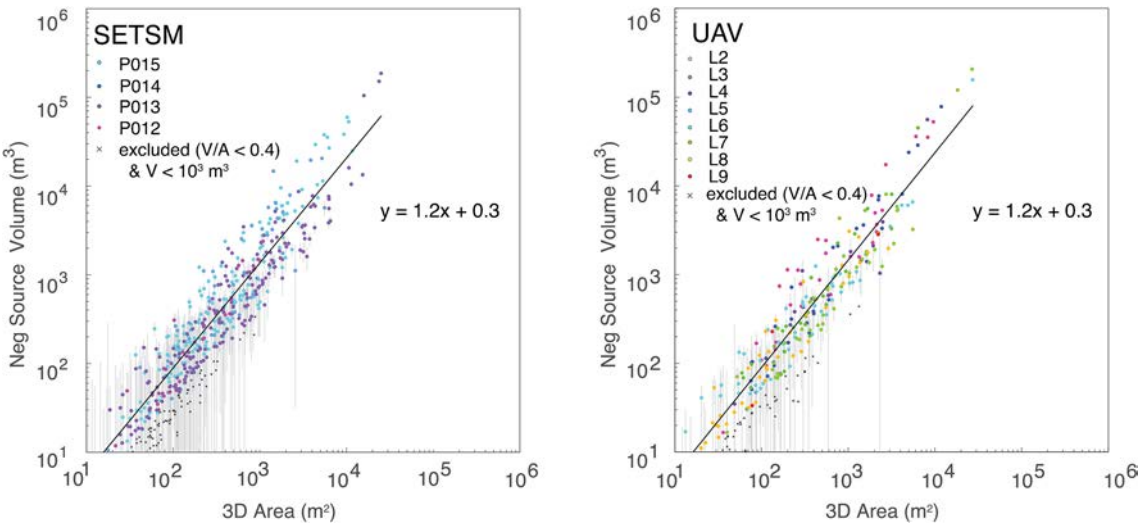

Fig. 12 Volume-area relationships for 2015 coseismic landslides by landslide SETSM scene or UAV region. Landslides with high volume uncertainty (V/A ratio < 0.4) are shown in grey and excluded from the regression analysis

The volume/area ratio, rather than elevation change or volume alone, was a more useful discriminate on limits of detection suggesting that thin rather than small landslides present a particular challenge. When DSM and difference model uncertainties are propagated into landslide volume uncertainty, we observe that landslides with volume/area ratios less than 0.4 show systematic and exponentially increasing error. When considering field and image interpretation, we suggest that these thin landslides are raveling or otherwise chaotic(?) surface displacements that are likely not coherent landslide movements and may also represent ongoing post-event slope changes. At this scale, we are running up against not a limit of technology and spatial resolution, but rather a limit in interpreting the landsliding process itself, which likely no longer conforms to defining simple, individual landslide geometries at a range of "landslide" areas. Further, other factors complicate interpretation of the smallest landslides in regional inventories. Probably the largest contributing factor is the time delay between before and after datasets and the likelihood of continued displacement of materials at the meter scale following the main shock of the earthquake. The issue of detection limits raises the question that the real cutoff may likely be a change in mechanism and unrelated to our technical ability to resolve surface change, and that change occurs not at a cutoff landslide area but rather depth and is best interpreted by image and field observation of slope behavior. These observations should prompt reconsideration of how we select the smallest landslide size for inclusion in regional landslide inventory statistics and how limits of detection are incorporated into automated 3D landslide mapping (Bernard et al. 2021).

Table 1 Log–log volume-area scaling parameters. Values are reported for slope and exponent values (γ, α). Bold values are shown in Figs. 11 and 12 with all plots with fits shown in Supplementary Fig. 4 and 5.

	Vol-2D area	*Vol-3D area*	*Vol-neg 3D area*
Full polygon—fit to entire population			
UAV	**1.0, 0.9**	1.0, 0.9	1.2, 0.3
SETSM	**1.0, 0.8**	1.0, 0.7	1.2, 0.3
Source polygon—fit to entire population			
UAV	1.1, 0.6	**1.1, 0.7**	1.2, 0.3
SETSM	1.1, 0.9	**1.1, 0.7**	1.2, 0.3
Full polygon—fit to $> 10^3$ m^2			
UAV	1.3, 0.1	1.2, 0.1	1.3, 0.1
SETSM	1.1, 0.4	1.2, 0.3	1.3, 0.1
Source polygon—fit to 10^3 m^2			
UAV	1.4, 0.1	1.4, 0.03	**1.6, 0.02**
SETSM	1.3, 0.1	1.3, 0.1	**1.4, 0.1**

The Lefkada event also provided an opportunity to advance landslide mapping protocols as well as assess several aspects of landslide mapping that have been speculated to affect event statistics, such as source vs. full area mapping, 2D vs. 3D area determination and amalgamation (Li et al. 2014; Marc and Hovius 2015; Massey et al. 2020a, b; Bernard et al. 2021). Additionally, we consider a summation of area only over the area of negative elevation change within the mapped polygon ("area of negative volume"). Subjective decisions made in the mapping process to address amalgamation also factors significantly into the determination of landslide frequency and commonly used statistics to measure and compare landslide events. Here we use a combination of features to define individual landslides within landslide complexes that include topographic features such as drainage divides and upslope contributing area, as well as visual features in the optical imagery of debris deposits. Doing so produces a log-normal distribution of landslide areas, and a censorship of both small and large landslide sizes, as is predicted by models considering the cohesion and depth dependent strength of near surface materials (e.g., (Frattini and Crosta 2013)) and the distribution of different hillslope lengths in a natural landscape (Medwedeff et al. 2020). We observe that differences in landslide event summary statistics in considering 2D versus 3D landslide area are negligible and are smaller than the slight differences between consideration of source versus full areas (Table 1). We note consideration of 3D area also introduces the complexity of scale, as the 3D area becomes exponentially larger for increasing DEM resolution. Thus, the measure of the 3D area for high-resolution datasets reflects in part, the roughness of the topographic surface rather than simply the difference between a slope-averaged area across a landslide compared to its 2D planform projection. Some thought as to the appropriate scale for averaging 3D slope values may improve results especially for individual landslides, but at present it seems to present a minor contribution to summary statistics measured across several orders magnitude scale. We find that consideration of the "area of negative volume" provided the greatest consistency in volume-area scaling, which we interpret to reflect a previously unrecognized aspect of determining landslide characteristics over a complicated failure surface.

In large landslide events, empirical V-A scaling relationships are typically coupled with 2D mapped landslide inventory data to project the total sediment volume mobilized by landslides during extreme events such as earthquakes and major storms (e.g., Li et al. 2014, 2017). To our knowledge, only two other regional earthquake landslide inventories exist that are based on direct differencing methods of before/after DEMs as in this study, both describing all or part of the 2016 M_w 7.8 Kaikoura earthquake event in New Zealand (Massey et al. 2020a, b; Bernard et al. 2021). This event triggered nearly 30,000 landslides and both used substantially more expensive deployment methods using either airborne orthophoto imagery or LiDAR. Compared to these studies, we derive similar volume-area scaling parameters when considering 2D area and the entire population of source polygons. However, when considering landslides $> 10^3$ m^3, we derive substantially higher slope exponents to the volume-area scaling relationship that reflect on average deeper landslides than observed in the Kaikoura example. We caution the determination of a single set of parameters to describe earthquake-triggered events, as the geologic condition and strength profile of the near surface environment likely significantly factors into this scaling. The methodology and completeness of landslide volume inventory presented here promises to improve these predictions by investigating controlling factors and selectively applying log area-volume parameters only to appropriately select the total landslide area. For example, the inclusion of shallow landslides (< 0.4 m average depth) and ravel that are not well captured by statistics reported from manual volume estimates from field methods, will likely overestimate total landslide volume. We note also that while commonly not emphasized in scaling studies, the alpha (log-intercept) can also have a large effect on estimating total event landslide volume. All of this is to emphasize the complexity of volume-area scaling parameters, and the sensitivity of these parameters to methodology, data quality, and representation across regional scales.

As more pre-event DEMs are becoming available, one significant challenge in using surface change detection for landslide events is the mixture of datasets (hybrid datasets) that may exist before and after the event, and the temporal proximity of those datasets to the event itself. DEM differencing from rapid deployment of UAV or satellite imagery coverage will also provide essential situational awareness during landslide disasters. Validation of satellite derived topography as presented here supports the use of such products as a cheaper and more readily available source of post-event topography for rapid response work to natural disasters, as well as the potential for research-grade datasets that may be more geographically distributed.

Conclusions

Optical data are constantly improving with advancements that allow for higher image resolution, ease of deployment or acquisition, and increases in the frequency of repeat measurement for which specific forcing of geomorphic change can be more confidently assigned.

Using two post-event datasets that were differenced from the same pre-event DEM allowed us to compare the resulting difference models as well as statistics of each independent difference model to assess the resulting 3D landslide inventory in terms of fidelity of measurement, minimum mapping resolution, and volume uncertainty. We find good agreement between DSM data types, which provides validation for the proposed methods for creating 3D landslide inventories. The UAV models performed with less variability (lower uncertainties) than the SETSM models likely due to better registration, higher resolution, and success of vegetation filtering programs.

The completeness and high resolution of the volume inventory allowed us to evaluate commonly cited statistics for landslide event inventories in new ways, such as exploring aspects of previous workflows that have been speculated to influence inventory scale statistics but not previously analyzed. These include analysis of source areas compared to full landslide areas, use of 2D (planview) landslide area versus 3D slope area, and amalgamation of adjacent landslides that coalesce into complicated landslide complexes. We demonstrate the sensitivity of statistical relationships to topographic resolution, accurate registration of before/after images, and estimation of 2D (plane) area versus 3D surface area. Across many portions of the inventory, our findings reveal complex patters of surface change that often are not well approximated by a simple landslide slip surface geometry and question the utility of landslide frequency as a statistical measure. These areas of shallow change account for a large percentage of the total landsliding area but have proportionally small contribution to the total landslide mass. When considering discrete landslide masses, if the highly uncertain shallow change is removed from the volume area relationship, we predict equal to larger total volumes than previous relationships based on field data alone. We also find that defining landslide areas as the areas where only volume loss was calculated, as opposed to the entire "source" area, significantly reduces scatter of the volume-area relationship. When restricting analysis to only the most frequent landslides and larger ($A = > 10^3$ m^2), produces a value ($\gamma = 1.3–1.4$) equal to the global value of rock rather than soil. This result challenges a commonly held notion that earthquake-triggered landslides are only shallow, and therefore do not contribute to landscape denudation by detachment of intact bedrock.

As we eliminate the selection bias of ground-based field studies that focus only on few, well-defined landslides and by enhancing 2D image-based landslide inventories to account for the magnitude of elevation change, new patterns of ground failure become evident and will require adaptation in mapping and statistical data interpretation.

Acknowledgements

Dr. Nikolas Middtun provided scientific illustration and scripting for the figures and development of the final GIS database. Dr. Christos Papaioanou from the Institute of Engineering Seismology & Earthquake Engineering (ITSAK, Greece) provided important strong motion data in the vicinity of the landslides. We thank (former) PhD students Weibing Gong and William Medwedeff and research assistant Logan Knoper, and our external collaborators; Dr. Harry Saroglou, Researcher at the Geotechnical Engineering Department of the National Technical University of Athens, and PhD student Vasilis Kalimogiannis; and Dr. Jonathan Godt (USGS). Paul Morin from the PGC (Polar Geospatial Center) provided imagery access and support for acquiring Digital Globe satellite data through a NGA (National Geospatial-Intelligence Agency) cooperative agreement with NSF (NextView License) which is supported by NSF grants OPP-1043681, OPP-1559691 and OPP-1542736. All satellite images are the copyright of Maxar, 2017.

Funding

This work was supported by the USGS NEHRP grant program (G17AP00088) to Zekkos and Clark, NASA Disasters Award 80NSSC19K0948 to Clark and NASA Disasters Award 80NSSC20K1032 to Zekkos.

Data Availability

The landslide inventory is made available via this pubilcation in the Supplementary Information. Additionally, the post-earthquake DSM UAV and SETSM models, difference models and PGA models used in this study are available through DesignSafe-CI Data Depot repository.

Declarations

Conflict of interest The authors declare no competing interests.

References

Abdullah NA, Nishioka D, Tanaka Y, Murayama Y (2015) User's action and decision making of retweet messages towards reducing misinformation spread during disaster. J Inform Processing 23(1):31–40

Alberti S, Leshchinsky B, Roering J, Perkins J, Olsen MJ (2022) Inversions of landslide strength as a proxy for subsurface weathering. Nat Commun 13(1):1–12

Alvioli M, Mondini AC, Fiorucci F, Cardinali M, Marchesini I (2018) Topography-driven satellite imagery analysis for landslide mapping. Geomat Nat Haz Risk 9(1):544–567

Amatya P, Kirschbaum D, Stanley T (2019) Use of very high-resolution optical data for landslide mapping and susceptibility analysis along the Karnali highway, Nepal. Remote Sensing 11(19):2284

Amatya P, Kirschbaum D, Stanley T, Tanyas H (2021) Landslide mapping using object-based image analysis and open source tools. Eng Geol 282:106000

Atwood A, West AJ (2022) Evaluation of high-resolution DEMs from satellite imagery for geomorphic applications: a case study using the SETSM algorithm. Earth Surf Proc Land 47(3):706–722

Barnard PL, Owen LA, Sharma MC, Finkel RC (2001) Natural and human-induced landsliding in the Garhwal Himalaya of northern India. Geomorphol 40(1–2):21–35

Bernard TG, Lague D, Steer P (2021) Beyond 2D landslide inventories and their rollover: synoptic 3D inventories and volume from repeat lidar data. Earth Surf Dyn 9(4):1013–1044

Bunn M, Leshchinsky B, Olsen MJ (2020) Geologic trends in shear strength properties inferred through three-dimensional back analysis of landslide inventories. J Geophysical Res: Earth Surface 125(9):e2019JF005461

Burrows K, Walters RJ, Milledge D, Spaans K, Densmore AL (2019) A new method for large-scale landslide classification from satellite radar. Remote Sensing 11(3):237

Catani F (2021) Landslide detection by deep learning of non-nadiral and crowdsourced optical images. Landslides 18(3):1025–1044

Corsa BD, Jacquemart M, Willis MJ, Tiampo KF (2022) Characterization of large tsunamigenic landslides and their effects using digital

surface models: a case study from Taan Fiord, Alaska. Remote Sens Environ 270:112881
Costa JE, Schuster RL (1988) The formation and failure of natural dams. Geol Soc Am Bull 100(7):1054–1068
Crosta G, Imposimato S, Roddeman D (2003) Numerical modelling of large landslides stability and runout. Nat Hazard 3(6):523–538
Dai CL, Durand M, Howat IM, Altenau EH, Pavelsky TM (2018) Estimating river surface elevation from ArcticDEM. Geophys Res Lett 45(7):3107–3114
Dai CL, Howat IM, Freymueller JT, Lu Z, Vijay S, Liljedahl AK, Jones MKW, Bergstedt H, Lev E (2022) Quantifying mass flows at Mt. Cleveland, Alaska between 2001 and 2020 using satellite photogrammetry. J Volcanol Geothermal Res 429.
Fan X, Dufresne A, Subramanian SS, Strom A, Hermanns R, Stefanelli CT, Hewitt K, Yunus AP, Dunning S, Capra L (2020) The formation and impact of landslide dams–state of the art. Earth Sci Rev 203:103116
Fonstad MA, Dietrich JT, Courville BC, Jensen JL, Carbonneau PE (2013) Topographic structure from motion: a new development in photogrammetric measurement. Earth Surf Proc Land 38(4):421–430
Frattini P, Crosta GB (2013) The role of material properties and landscape morphology on landslide size distributions. Earth Planet Sci Lett 361:310–319
Gabet EJ, Dunne T (2002) Landslides on coastal sage-scrub and grassland hillslopes in a severe El Nino winter: the effects of vegetation conversion on sediment delivery. Geol Soc Am Bull 114(8):983–990
Ganas A, Elias P, Bozionelos G, Papathanassiou G, Avallone A, Papastergios A, Valkaniotis S, Parcharidis I, Briole P (2016) Coseismic deformation, field observations and seismic fault of the 17 November 2015 M=6.5, Lefkada Island, Greece earthquake. Tectonophysics 687:210–222
Ganas A, Briole P, Papathanassiou G, Bozionelos G, Avallone A, Melgar D, Argyrakis P, Valkaniotis S, Mendonidis E, Moshou A (2015) A preliminary report on the Nov 17, 2015 M= 6.4 South lefkada earthquake, Ionian Sea, Greece. Report published online on EMSC. https://www.earthquakegeology.com/materials/reports/Lefkada_17_Nov_2015-Earthquake_Report.pdf. Accessed 10/28/2024
Gong W, Zekkos D, Clark M, Manousakis J, Kirshbaum D (2021) Regional 3D stability analyses of the Egkremnoi coastline and comparison with landslides caused by the 2015 Lefkada earthquake. IFCEE 2021:130–138
Gong W, Zekkos D, Clark M (2023) A pseudo-3D methodology for regional-scale back-analysis of earthquake-induced landslides. Eng Geol 325:107277
Guzzetti F, Malamud BD, Turcotte DL, Reichenbach P (2002) Power-law correlations of landslide areas in central Italy. Earth Planet Sci Lett 195(3–4):169–183
Hölbling D, Eisank C, Albrecht F, Vecchiotti F, Friedl B, Weinke E, Kociu A (2017) Comparing manual and semi-automated landslide mapping based on optical satellite images from different sensors. Geosciences 7(2):37
Hovius N, Stark CP, Allen PA (1997) Sediment flux from a mountain belt derived by landslide mapping. Geology 25(3):231–234
Hungr O, Leroueil S, Picarelli L (2014) The Varnes classification of landslide types, an update. Landslides 11(2):167–194
Imaizumi F, Sidle RC (2007) Linkage of sediment supply and transport processes in Miyagawa Dam catchment, Japan. J Geophysical Res-Earth Surface 12:F03012
Jeandet L, Steer P, Lague D, Davy P (2019) Coulomb mechanics and relief constraints explain landslide size distribution. Geophys Res Lett 46(8):4258–4266
Jones K, Howarth J, Massey CI, Sirguey P, Lague D, Bernard T (2023) Accurate quantification of sediment conveyance following the 2016 Kaikōura earthquake, New Zealand. EGU General Assembly, Vienna, Austria, EGU:4588
Kallimogiannis V, Saroglou C, Zekkos D, Manousakis J (2019) 2D and 3D Back-analysis of a landslide in Egremnoi caused by the November 17 2015 Lefkada earthquake. 2nd International Conference on Natural Hazards & Infrastructure in Chania, Greece
Kerle N (2002) Volume estimation of the 1998 flank collapse at Casita volcano, Nicaragua: a comparison of photogrammetric and conventional techniques. Earth Surf Proc Land 27(7):759–772
King MD, Howat IM, Candela SG, Noh MJ, Jeong S, Noël BPY, van den Broeke MR, Wouters B, Negrete A (2020) Dynamic ice loss from the Greenland Ice Sheet driven by sustained glacier retreat. Commun Earth Environ 1(1):11–77
Lacroix P (2016) Landslides triggered by the Gorkha earthquake in the Langtang valley, volumes and initiation processes. Earth Planets and Space 68(1):1–10
Larsen IJ, Montgomery DR, Korup O (2010) Landslide erosion controlled by hillslope material. Nat Geosci 3(4):247–251
Li G, West AJ, Densmore AL, Jin ZD, Parker RN, Hilton RG (2014) Seismic mountain building: landslides associated with the 2008 Wenchuan earthquake in the context of a generalized model for earthquake volume balance. Geochem Geophys Geosyst 15(4):833–844
Li G, West AJ, Densmore AL, Jin Z, Zhang F, Wang J, Clark M, Hilton RG (2017) Earthquakes drive focused denudation along a tectonically active mountain front. Earth Planet Sci Lett 472:253–265
Lucieer A, de Jong SM, Turner D (2014) Mapping landslide displacements using structure from motion (SfM) and image correlation of multitemporal UAV photography. Progress Physical Geography-Earth and Environment 38(1):97–116
Malamud BD, Turcotte DL, Guzzetti F, Reichenbach P (2004) Landslides, earthquakes, and erosion. Earth Planet Sci Lett 229(1–2):45–59
Mancini F, Dubbini M, Gattelli M, Stecchi F, Fabbri S, Gabbianelli G (2013) Using unmanned aerial vehicles (UAV) for high-resolution reconstruction of topography: the structure from motion approach on coastal environments. Remote Sensing 5(12):6880–6898
Marc O, Hovius N (2015) Amalgamation in landslide maps: effects and automatic detection. Nat Hazard 15(4):723–733
Marc O, Hovius N, Meunier P, Uchida T, Hayashi S (2015) Transient changes of landslide rates after earthquakes. Geology 43(10):883–886
Martha TR, Kerle N, Jetten V, van Westen CJ, Kumar KV (2010) Landslide volumetric analysis using Cartosat-1-derived DEMs. IEEE Geosci Remote Sens Lett 7(3):582–586
Massey C, Townsend D, Lukovic B, Morgenstern R, Jones K, Rosser B, de Vilder S (2020a) Landslides triggered by the M_w7. 8 14 November 2016 Kaikōura earthquake: an update. Landslides 17(10):2401–2408
Massey CI, Townsend D, Jones K, Lukovic B, Rhoades D, Morgenstern R, Rosser B, Ries W, Howarth J, Hamling I, Petley D, Clark M, Wartman J, Litchfield N, Olsen M (2020b) Volume characteristics of landslides triggered by the MW 7.8 2016 Kaikōura Earthquake, New Zealand, derived from digital surface difference modeling. J Geophysical Res: Earth Surface 125(7):e2019JF005163
May CL (2002) Debris flows through different forest age classes in the central Oregon Coast Range. J Am Water Resour Assoc 38(4):1097–1113
McDougall S (2017) 2014 Canadian Geotechnical Colloquium: landslide runout analysis—current practice and challenges. Can Geotech J 54(5):605–620
Medwedeff WG, Clark MK, Zekkos D, West AJ (2020) Characteristic landslide distributions: an investigation of landscape controls on landslide size. Earth Planet Sci Lett 539:116203
Medwedeff WG, Clark MK, Zekkos D, West AJ, Chamlagain D (2022) Near-surface geomechanical properties and weathering characteristics across a tectonic and climatic gradient in the central Nepal Himalaya. J Geophysical Res: Earth Surface 127(2):e2021JF006240
Melling L, Leeson A, McMillan M, Maddalena J, Bowling J, Glen E, Sorensen LS, Winstrup M, Arildsen RL (2024) Evaluation of satellite methods for estimating supraglacial lake depth in southwest Greenland. Cryosphere 18(2):543–558
Miele P, Di Napoli M, Guerriero L, Ramondini M, Sellers C, Annibali Corona M, Di Martire D (2021) Landslide awareness system (LAwS) to increase the resilience and safety of transport infrastructure: the case study of Pan-American Highway (Cuenca–Ecuador). Remote Sensing 13(8):1564
Niethammer U, James MR, Rothmund S, Travelletti J, Joswig M (2012) UAV-based remote sensing of the Super-Sauze landslide: evaluation and results. Eng Geol 128:2–11

Nissen E, Krishnan AK, Arrowsmith JR, Saripalli S (2012) Three-dimensional surface displacements and rotations from differencing pre- and post-earthquake LiDAR point clouds. Geophysical Res Lett 39:L16301
Noh MJ, Howat IM (2015) Automated stereo-photogrammetric DEM generation at high latitudes: surface extraction with TIN-based search-space minimization (SETSM) validation and demonstration over glaciated regions. Gisci Remote Sensing 52(2):198–217
Noh MJ, Howat IM (2017) The surface extraction from TIN based search-space minimization (SETSM) algorithm. ISPRS J Photogramm Remote Sens 129:55–76
Postance B, Hillier J, Dijkstra T, Dixon N (2017) Extending natural hazard impacts: an assessment of landslide disruptions on a national road transportation network. Environ Res Lett 12(1):014010
Roback K, Clark MK, West AJ, Zekkos D, Li G, Gallen SF, Chamlagain D, Godt JW (2018) The size, distribution, and mobility of landslides caused by the 2015 Mw7.8 Gorkha earthquake, Nepal. Geomorphology 301:121–138
Schenk T (1999) Digital Photogrammetry. Laurelville, OH: TerraScience. p 429
Snavely N, Seitz SM, Szeliski R (2008) Modeling the world from Internet photo collections. Int J Comput Vision 80(2):189–210
Tanyas H, van Westen CJ, Allstadt KE, Jessee MAN, Gorum T, Jibson RW, Godt JW, Sato HP, Schmitt RG, Marc O, Hovius N (2017) Presentation and analysis of a worldwide database of earthquake-induced landslide inventories. J Geophysical Res-Earth Surface 122(10):1991–2015
Tanyaş H, Allstadt KE, van Westen CJ (2018) An updated method for estimating landslide-event magnitude. Earth Surf Proc Land 43(9):1836–1847
Teza G, Galgaro A, Zaltron N, Genevois R (2007) Terrestrial laser scanner to detect landslide displacement fields: a new approach. Int J Remote Sens 28(16):3425–3446
Tsutsui K, Rokugawa S, Nakagawa H, Miyazaki S, Cheng CT, Shiraishi T, Yang SD (2007) Detection and volume estimation of large-scale landslides based on elevation-change analysis using DEMs extracted from high-resolution satellite stereo imagery. IEEE Trans Geosci Remote Sens 45(6):1681–1696
Ullman S (1979) Interpretation of structure from motion. Proceedings Royal Soc Series B-Biol Sci 203(1153):405–426
Valagussa A, Marc O, Frattini P, Crosta G (2019) Seismic and geological controls on earthquake-induced landslide size. Earth Planet Sci Lett 506:268–281
Varnes DJ (1978) Slope movement types and processes. Special Report 176:11–33
Westoby MJ, Brasington J, Glasser NF, Hambrey MJ, Reynolds JM (2012) 'Structure-from-motion' photogrammetry: a low-cost, effective tool for geoscience applications. Geomorphology 179:300–314
Wieczorek GF, Wilson RC, Harp EL (1985) Map showing slope stability during earthquakes in San Mateo County, California. No. 1257-E
Zekkos D, Clark M, Cowell K, Medwedeff W, Manousakis J, Saroglou H, Tsiambaos G (2017) Satellite and UAV-enabled mapping of landslides caused by the November 17th 2015 Mw 6.5 Lefkada earthquake. In: Proceedings 19th Int. Conference on soil mechanics and geotechnical engineering. Seoul, Korea, pp 2235–2238
Zekkos D, Clark M, Willis M, Athanasopoulos-Zekkos A, Manousakis J, Knoper L, Stahl T, Massey CI, Archibald G, Greenwood W, Medwedeff W (2018a) 3D models of the Leader Valley using satellite & UAV imagery following the 2016 Kaikoura earthquake. 11th US National Conference on Earthquake Engineering.
Zekkos D, Clark MK (2019) USGS NEHRP Final Technical Reports, USGS. https://earthquake.usgs.gov/cfusion/external_grants/reports/G17AP00088.pdf. Accessed 10/28/2024
Zekkos D, Greenwood W, Lynch J, Manousakis J, Athanasopoulos-Zekkos A, Clark M, Cook KL, Saroglou C (2018b) Lessons learned from the application of UAV-enabled structure-from-motion photogrammetry in geotechnical engineering. Int J Geoeng Case Hist 4(4):254–274

Supplementary Information The online version contains supplementary material available at https://doi.org/10.1007/s10346-024-02374-x.

Marin K. Clark (✉)
Department of Earth and Environmental Sciences, Univ. of Michigan, 1100 North University Ave., Ann Arbor, MI 48109, USA

Marin K. Clark
Email: marinkc@umich.edu

Dimitrios Zekkos
Department of Civil and Environmental Engineering, Univ. of California at Berkeley, 425 Davis Hall, Berkeley 94720, CA, USA

John Manousakis
ARGO-E Group, 54 Vas. Sophias Av., 11528 Athens, GR, Greece